Nature Communications

https://doi.org/10.1038/s41467-026-74811-5

Article in Press

Negative temperature coefficient metamaterial absorber for uniform microwave heating

Received: 8 May 2025

Accepted: 16 June 2026

Published online: 27 June 2026

Cite this article as: Zhou, J., Li, D., Xia, L. *et al.* Negative temperature coefficient metamaterial absorber for uniform microwave heating. *Nat Commun* (2026). https://doi.org/10.1038/s41467-026-74811-5

Jing Zhou, Di Li, Lingfeng Xia, Xicheng Heng, Shuting Liu, Guido Link, James Gao, Xiaozhong Hao, Lei Zhou & Yingguang Li

Negative temperature coefficient metamaterial absorber for uniform microwave heating

Jing Zhou[1†], Di Li[1†], Lingfeng Xia[1], Xicheng Heng[1], Shuting Liu[1], Guido Link[2], James Gao[1,3], Xiaozhong Hao[1], Lei Zhou[4,5], Yingguang Li[1*]

[1]College of Mechanical and Electrical Engineering, Nanjing University of Aeronautics and Astronautics, Nanjing, 210016, China.

[2]Karlsruhe Institute of Technology (KIT), Hermann-von-Helmholtz-Platz 1, 76344 Eggenstein-Leopoldshafen, Germany.

[3]School of Engineering, University of Greenwich, Chatham Maritime, Kent ME4 4TB, UK.

[4]State Key Laboratory of Surface Physics, Key Laboratory of Micro and Nano Photonic Structures (MOE), and Department of Physics, Fudan University, Shanghai, 200433, China.

[5]Shanghai Key Laboratory of Metasurfaces for Light Manipulation, Fudan University, Shanghai, 200433, China.

[*]Corresponding author. e-mail: liyingguang@nuaa.edu.cn

[†]These authors contributed equally: Jing Zhou, Di Li.

ABSTRACT Microwave heating is widely used in daily applications but is fundamentally limited by non-uniform temperature distribution. Despite extensive efforts to manipulate energy distribution around materials, achieving uniform heating remains elusive due to the intrinsic inhomogeneity of electromagnetic fields. Here, we report a self-regulating solution that adaptively modulates the absorbance distribution using a *Negative Temperature Coefficient* (NTC) *Metamaterial Absorber* (MA). Distinct from electromagnetic field-shaping strategies, our approach intrinsically suppresses overheating in high-temperature regions and redistributes energy to cooler areas. We demonstrate, for the first time, that uniform heating—quantified by over 90% reduction in the coefficient of variation—can be achieved across diverse configurations, including planar, polyhedral, curved, and multiple objects, as well as under power variations spanning two orders of magnitude. This work not only provides a theoretical resolution to the longstanding challenge of non-uniform microwave heating but also opens new avenues for development and application of temperature-adaptive metamaterials.

Introduction

Since the 1960s, microwave heating technology has emerged as a promising thermal processing method due to its advantages of rapid, volumetric, and selective heating [1-4]. Today, its applications have expanded into various fields closely tied to everyday life such as food processing [5,6], chemical catalysis [7,8], materials synthesis or processing [9-11], waste treatment [12,13], environmental engineering [14,15], energy industry [16,17], and biomedical applications [18,19]. However, for decades, longstanding challenges arising from inherent non-uniform heating patterns have not only affected user experience in existing applications but also limited the technology's potential in advanced applications [20-22]. To address this issue, numerous efforts have been devoted to manipulating the electromagnetic field around materials [23-30]. Representative strategies—including rotating turntables, mode stirring, and conveyor-assisted motion averaging—have achieved practical success in applications with moderate uniformity requirements and cost constraints. Nevertheless, realizing a genuinely uniform microwave field remains intrinsically challenging, as microwave antennas exhibit specific radiation patterns, while resonant cavities support discrete modes of microwaves, both of which naturally lead to spatial variations in field intensity rather than a uniform distribution.

Theoretically, the temperature distribution is governed by the interaction between the material and the electromagnetic field, thereby retaining the possibility of controlling the temperature field via the material's absorption characteristics. Motivated by this perspective, here we investigate the feasibility of improving temperature uniformity by dynamically tailoring the spatial absorbance distribution. In recent years, metamaterial absorbers (MAs) have attracted widespread interest due to their flexibly tunable absorption properties [31-37]. A typical MA structure consists of a layer of patterned metallic units and a conductive substrate, separated by a dielectric spacer. Its microwave absorption can be easily tuned by engineering the characteristics of constituent materials and by adjusting geometric parameters [38-47]. Building on these unique advantages, we propose a negative temperature coefficient (NTC) MA capable of adaptively redistributing microwave absorption during heating, thereby enabling self-regulated

homogenization of the temperature field. A detailed description of the design framework and operating mechanism of the NTC MA is provided in **Supplementary Note 1**.

As schematically illustrated in **Figure 1a**, the MA used in this work also features a sandwich structure and exhibits narrowband absorption, with a resonant frequency of f_{res}. The NTC absorption is achieved by designing the temperature-dependent permittivity (ε_r) of the dielectric spacer. According to the equivalent circuit model [48], the relationship between f_{res} and ε_r satisfies $f_{res} \propto 1/\sqrt{\varepsilon_r}$. Thus, as long as ε_r changes monotonically with temperature T, f_{res} will also vary monotonically with T. In this work, as shown in **Figure 1b**, ε_r is designed to decrease with T, and thus f_{res} is positively correlated with T. Initially, when microwave power is applied at a frequency of f_{wave1}, the absorbance reaches nearly 100% at a lower temperature (T_1), but gradually decreases to a very low level at a higher temperature (T_2), thereby achieving NTC microwave absorption. If we want to further heat the material, the frequency of the microwave power can be adjusted to f_{wave2}, which matches the MA's resonant frequency at T_3, thereby restoring strong microwave absorption for the subsequent NTC heating process.

Through NTC microwave absorption, a self-regulating mechanism can be achieved, as illustrated in **Figure 1c**. When exposed to an uneven electromagnetic field, a non-uniform temperature field is generated, which activates the MA's NTC absorption response. Specifically, regions with higher temperatures exhibit reduced absorption, while cooler areas retain higher microwave absorbance, adaptively generating a complementary absorbance distribution. As a consequence, the temperature distribution across the MA will eventually become uniform. Furthermore, in microwave cavities, the selective heating nature of microwaves preferentially redirects energy toward higher absorbance regions (i.e., cooler areas), further accelerating the convergence toward a uniform temperature distribution (**Figure 1d**). As shown in **Figure 1e**, uniform heating has been achieved in both simulations and experiments for NTC MAs, even when some faces of the polyhedron are oriented away from the wave

port. This stands in stark contrast to conventional MAs, which exhibit constant microwave absorption. **Figure 1f** further demonstrates the potential of the NTC MA for programmable, pattern-selective uniform heating. It can be observed that the temperature distribution sequentially forms the Chinese characters "一", "十", and "田" (meaning "one," "ten," and "field," respectively). At each stage, uniform temperature within the target pattern is maintained, owing to the NTC absorption effect.

Practically, the proposed NTC MA can be integrated with both conductive and dielectric target materials, functioning either as the conductive substrate or as part of the dielectric spacer, thereby enabling adaptive regulation of local microwave absorption while preserving the intrinsic advantages of volumetric microwave heating. More generally, the NTC MA may also be implemented as an ultrathin functional film laminated onto object surfaces for indirect heating applications. In this configuration, electromagnetic energy is primarily absorbed and redistributed by the NTC MA layer rather than by the object itself, thus avoiding object-specific electromagnetic redesign and enabling compatibility with a broad range of materials, including those with intrinsically weak microwave absorbance. As a complementary strategy to established field-engineering approaches such as rotating turntables and mode stirring, the proposed absorption-control strategy may be particularly valuable in advanced manufacturing scenarios where stringent temperature uniformity is essential, including high-performance fabrication of composite structures, high-precision processing of dielectric components, and high-value treatment of biomedical products.

In the following sections, we first investigate two primary mechanisms for improving temperature uniformity: (i) suppressing temperature rise in hot regions (high field strength) and (ii) enhancing temperature rise in cold regions (low field strength). Guided by these mechanisms, we design an NTC MA and validate its effectiveness in improving temperature uniformity through both simulations and experiments. Finally, we present a representative application and a limit analysis of the NTC MA.

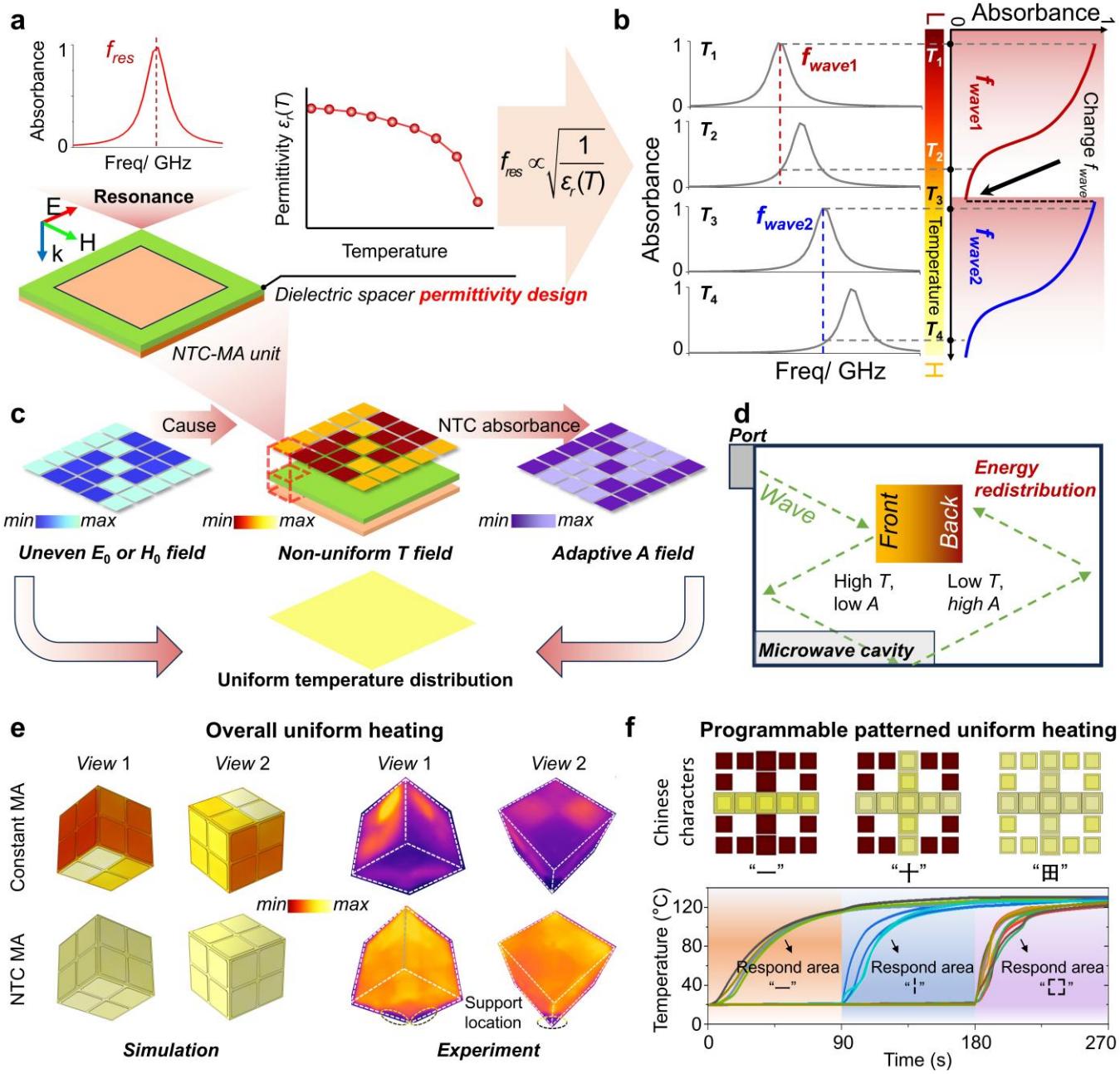

Figure 1| Schematic illustration of the NTC MA and its contribution to improving microwave heating uniformity. a The adopted sandwich MA unit with a thermosensitive dielectric spacer. **b** Realization of NTC absorption through temperature-dependent absorption peaks. **c** Uniform microwave heating resulted from the adaptively complementary absorbance distribution. **d** Preferential energy redistribution to cooler areas under the selective heating effect of microwaves. **e** Comparison of heating uniformity in both simulation and experiment between MAs with constant absorption and NTC absorption. **f** Programmable pattern-selective uniform heating enabled by NTC MAs.

Results and Discussion

Theoretical analysis of temperature distribution influenced by NTC absorption

Theoretical analysis was first conducted on a series of representative NTC absorbance cases. In classical electromagnetism, information about microwave absorbance is inherently embedded within physical parameters such as material thickness, complex permittivity, and complex permeability [49,50], making it difficult to directly isolate and analyze the impact of the absorbance distribution. In this study, we establish an explicit mathematical relationship among the temperature field $T(\vec{r})$, absorbance distribution $A(\vec{r})$, and external electromagnetic field $E_0(\vec{r})$ or $H_0(\vec{r})$, under the assumption that microwaves are incident on the top surface (at arbitrary point $\vec{r}$) of the thin NTC MA, with no transmission through the bottom surface and negligible edge effects.

$$\frac{\mathrm{d}T(\vec{r})}{\mathrm{d}t} \propto A(\vec{r})E_0^2(\vec{r}) \text{ or } A(\vec{r})H_0^2(\vec{r}) \tag{1}$$

The corresponding derivation is provided in **Supplementary Note 2**. Accordingly, the temperature field is determined by both the absorbance distribution and the external electromagnetic (EM) field from the MA. However, in practical multimode cavity applications, variations in material absorbance inherently cause EM field redistribution, which poses significant challenges for isolating the effects of NTC characteristics on the temperature field. To address this complexity, a two-stage analysis is adopted in this study. In the first stage, the effects of EM field redistribution are eliminated to investigate the influence of fundamental NTC characteristics. In the second stage, the impact of NTC absorbance on EM field variation (i.e., the EM field redistribution effect) is examined.

Influence of pure NTC absorption characteristics. The absorbance-temperature (*A*–*T*) profile can be characterized by three NTC features: (i) the initial absorbance A_0, (ii) the decline amplitude $\Delta A = A_0 - A_1$, and (iii) the decline pattern $\mathrm{d}A/\mathrm{d}T$ (e.g., fast-to-slow or slow-to-fast), where A_1 denotes the final

absorbance at the target temperature. A theoretical analysis was performed to investigate the influence of these three NTC characteristics on the evolution of the temperature field, assuming a fixed power density ratio of 8:1 between the high-power and low-power regions. Meanwhile, the coefficient of variation (COV, defined as the standard deviation over the mean) was employed to quantify the temperature uniformity [29]. The detailed mathematical framework for several representative cases supporting this analysis is provided in **Supplementary Note 3**.

The impact of the initial absorbance is investigated in **Figure 2a**. The initial absorbance A_0 at room temperature (around 25 °C) is set as 1, 0.66 and 0.33, while the absorbance decreases linearly with a fixed decline amplitude ΔA of 0.33. It can be observed that the temperature profiles remain divergent throughout the process as long as the final absorbance $A_1 \neq 0$. However, in the case of $A_0 = 0.33$ and $A_1 = 0$, full temperature convergence is achieved. The COV initially increases due to the uneven power distribution, but then drops rapidly as the temperature in the high-power region approaches the target temperature, triggering a self-limiting heating behavior and allowing the low-power region to catch up. **Figure 2b** depicts the result for different absorbance decline amplitudes. Similarly, full convergence can only be achieved when $A_1 = 0$. Compared with the $A_0 = 0.33$ group in **Figure 2a**, the temperature convergence is significantly accelerated, with the time required for full convergence reduced from 3150 s to 1185 s, indicating that a large absorbance decline amplitude is favorable for achieving temperature uniformity. **Figure 2c** shows the result for different absorbance decline patterns, with the initial and final absorbance fixed at $A_0 = 1$ and $A_1 = 0$, respectively. It can be seen that, as the area enclosed by the *A*–*T* curve and the coordinate axes increases from *Case* 1 to *Case* 3, the temperature convergence rate progressively accelerates, with the time required for full convergence decreasing from above 10,000 s to 780 s. This implies that, in the absence of EM field variations, the optimal *A*–*T* curve would ideally exhibit a stepwise change from 1 to 0 at the target temperature.

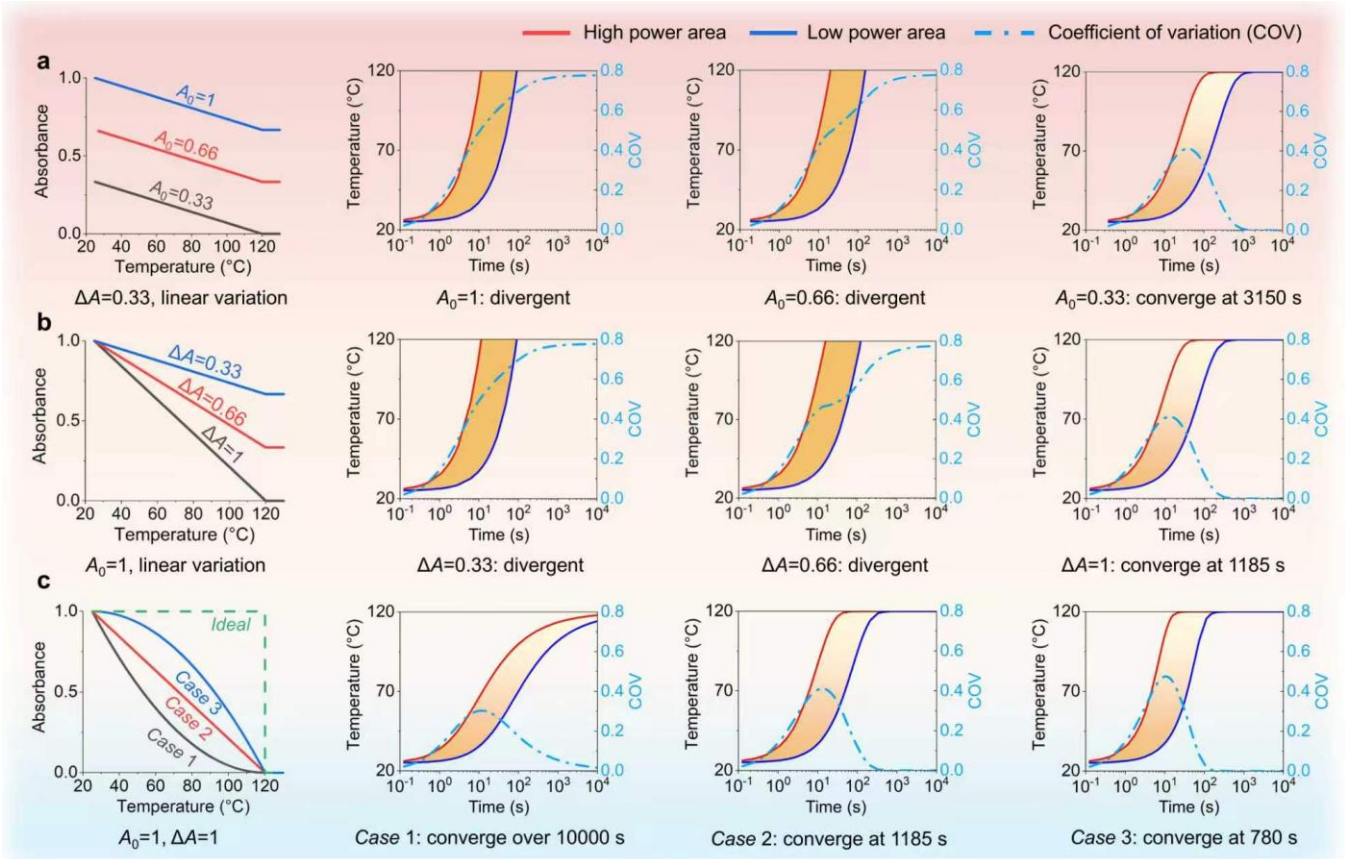

Figure 2| Influence of pure NTC absorption on heating uniformity. a Influence of the initial absorbance. **b** Influence of absorbance decline amplitudes. **c** Influence of absorbance decline patterns.

Taking EM field redistribution effect into account. For multimode microwave cavities, which are widely used in practical applications, EM field redistribution—induced by variations in microwave absorption—plays a crucial role in shaping the temperature distribution. As illustrated in **Figure 3a**, when two heating targets with identical microwave absorbance are placed in two different regions of the cavity, the absorbed power in, for example, *Zone* 2 may be significantly higher than that in *Zone* 1 due to the extremely uneven power distribution. Consequently, the temperature in *Zone* 2 rises much faster than that in *Zone* 1. With continued heating, the NTC effect causes the absorbance of *Zone* 2 to decrease to a low level, giving rise to a reflective behavior, whereas the absorbance in *Zone* 1 remains high and thus sustains strong microwave absorption (see **Figure 3b**). In this case, the energy reflected from *Zone* 2 will preferentially redistribute toward *Zone* 1, further accelerating the temperature convergence between the two regions. It should be noted, however, that part of the reflected energy may also propagate back toward

the microwave source through the wave port. This issue can be effectively mitigated by employing an asymmetric waveguide configuration [49,52].

To quantitatively investigate the EM field redistribution effect, we performed a series of simulations using MAs whose microwave absorbance can be flexibly tuned by tailoring the properties of the constituent materials and the geometric parameters of the structure. The methodology involved deliberately reducing the absorbance of the high-power region while maintaining the high absorbance of the low-power region, followed by monitoring the absorbed power of each MA unit. Under such conditions, any variation in absorbed energy within the low-power region originates solely from changes in its local EM field. As shown in **Figure 3c**, a planar MA composed of nine units was placed at the center of a cubic microwave cavity with a side length of 300 mm. Initially, the absorbance of each MA unit was set to $A = 0.95$, and the resulting absorbed power distribution—represented by the electric field magnitude in the dielectric spacer—reveals distinct low-power (*Zone* 1) and high-power (*Zone* 2) regions.

Subsequently, four additional simulations were carried out by decreasing the absorbance in *Zone* 2 (A_2) to 0.75, 0.40, 0.20, and 0.05, while keeping the absorbance in *Zone* 1 (A_1) fixed at 0.95. More simulation details are provided in **Supplementary Note 4**. It can be seen from **Figure 3c** and **3d** that as A_2 decreases from 0.95 to 0.05, the power absorbed by each unit in *Zone* 2 decreases significantly, while the energy absorbed by the units in *Zone* 1 increases markedly, indicating a pronounced EM field redistribution effect. As shown in **Figure 3e**, the case with $A_2 \approx 0.6$ represents a critical state. Before this point, *Zone* 2's unit absorbs more power than *Zone* 1's, leading to a faster temperature rise and thus a pronounced temperature difference between the two regions. Beyond this point, however, *Zone* 2's unit absorbs less power than *Zone* 1's, resulting in a slower temperature increase that helps reduce the temperature difference. Remarkably, when A_2 is reduced to 0.20, the average power absorbed by the unit in *Zone* 2 drops to about 12% of its original value, while that in *Zone* 1 increases to approximately 7.2 times its initial value due to the EM field redistribution effect. This phenomenon is particularly

advantageous, as it demonstrates that complete suppression of microwave absorption in the high-power region is unnecessary—a substantial reduction in absorbance (e.g., from 1 to 0.20) is sufficient to trigger strong field redistribution, which is more feasible for practical implementation. However, it can also be observed that the total power absorbed by the whole MA (i.e., normalized load loss) decreases as A_2 decreases, accompanied by increasing reflection of power back to the microwave source (see **Figure 3f**). Quantitatively, when A_2 decreases to 0.20, approximately 35% of the incident energy is reflected back to the source. The feasibility of reducing wave-port reflection via an asymmetric waveguide is demonstrated in **Supplementary Note 5**.

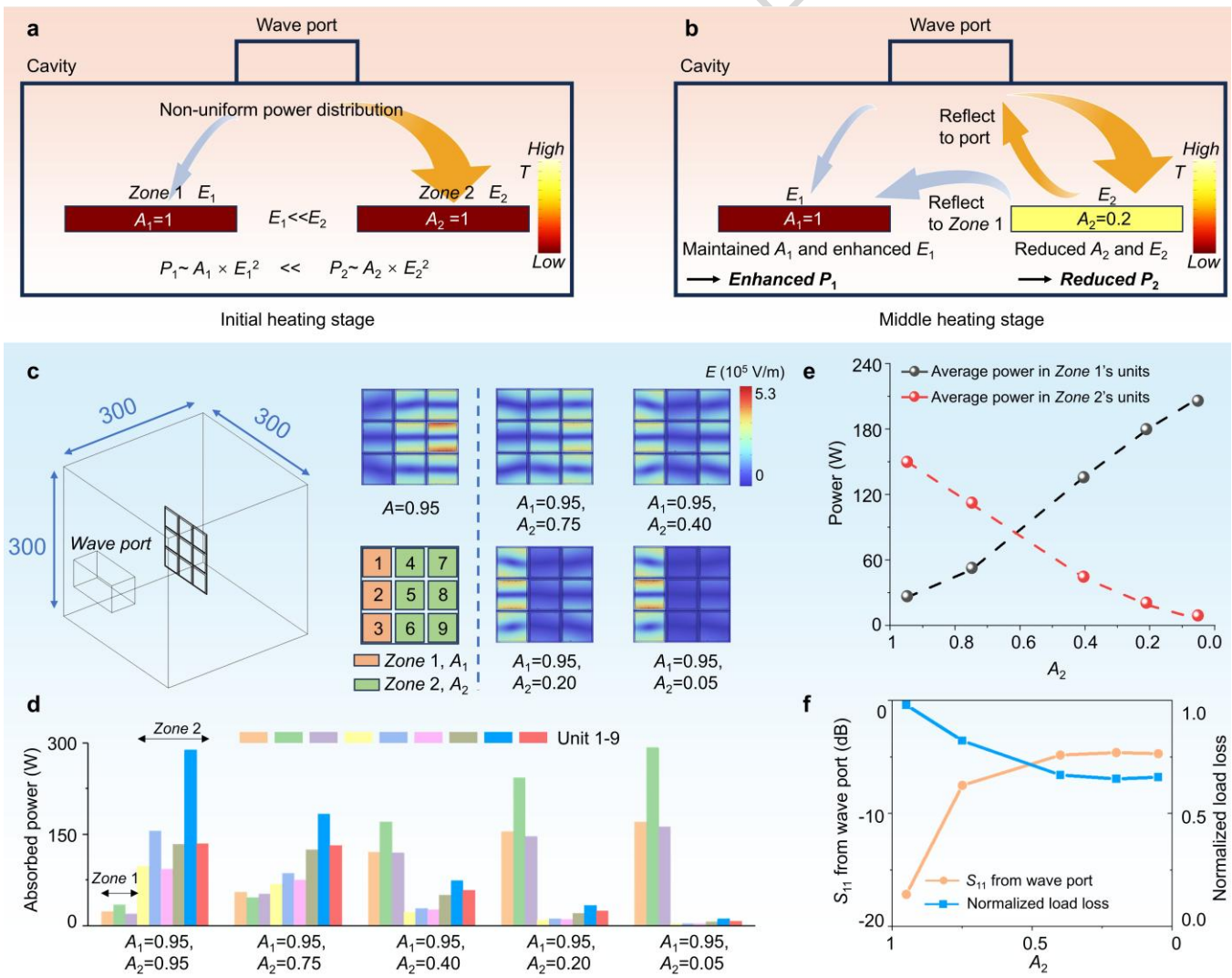

Figure 3| EM field redistribution induced by NTC absorption in multimode cavities. a Schematic of uneven power distribution in the microwave cavity. **b** Power redistribution induced by variations in

material absorbance. **c** Simulation setup and electric field magnitude in the dielectric spacer for different absorbance distributions. **d** Absorbed power of individual MA units under varying absorbance distributions. **e** Average power absorbed by units in *Zone* 1 and *Zone* 2. **f** Reflection loss (S_{11}) at the wave port and normalized load loss.

Validation of enhanced heating uniformity through NTC absorption

A series of simulations, followed by experimental validation, were conducted to validate the effectiveness of the proposed method by comparatively analyzing two representative cases: one involving a constant MA as a benchmark (*Scenario* 1), and the other utilizing an NTC MA developed in this work (*Scenario* 2). Guided by the theoretical framework above, the desired *A*–*T* response was engineered through an NTC MA incorporating a thermosensitive dielectric spacer and careful selection of the operating microwave frequency (see **Figure 4a**). The ideal step-like *A*–*T* profile was not adopted, as abrupt phase-change dielectric spacers—such as vanadium dioxide—feature intrinsically low phase-transition temperatures, which currently limit their applicability. In addition, the residual absorbance (9.3%) of the NTC MA at the target temperature originates from the intrinsic loss of the dielectric spacer, which, as discussed above, does not undermine the heating uniformity owing to the assistance of the EM field redistribution effect. Detailed simulation settings can be found in **Supplementary Note 4**.

The simulation results for a planar MA with 5 × 5 units are presented in **Figure 4b-f**. As observed, *Scenario* 1 exhibits continuously divergent temperature profiles due to the uneven electromagnetic field, while *Scenario* 2 shows profiles that initially diverge but gradually converge toward the target temperature, achieving a reduction of 92% in COV. Notably, in contrast to the non-intersecting temperature profiles depicted in **Figure 4b**, the temperature curves in **Figure 4c** exhibit pronounced intersections. This behavior arises because, unlike the static and uneven heating pattern in *Scenario* 1, *Scenario* 2 features an adaptive heating pattern (see **Figure 4d**), where local heating rates dynamically adjust in response to temperature evolution. More intuitively, as shown in **Figure 4e-f** and **Supplementary Movie 1**, the uneven and static electromagnetic field pattern under *Scenario* 1 leads to an increasingly non-uniform temperature distribution. In contrast, *Scenario* 2 exhibits a dynamic redistribution of electromagnetic

fields, contributing to almost uniform temperature distribution—even though the initial power distribution across the planar NTC MA units spans two orders of magnitude (1:267).

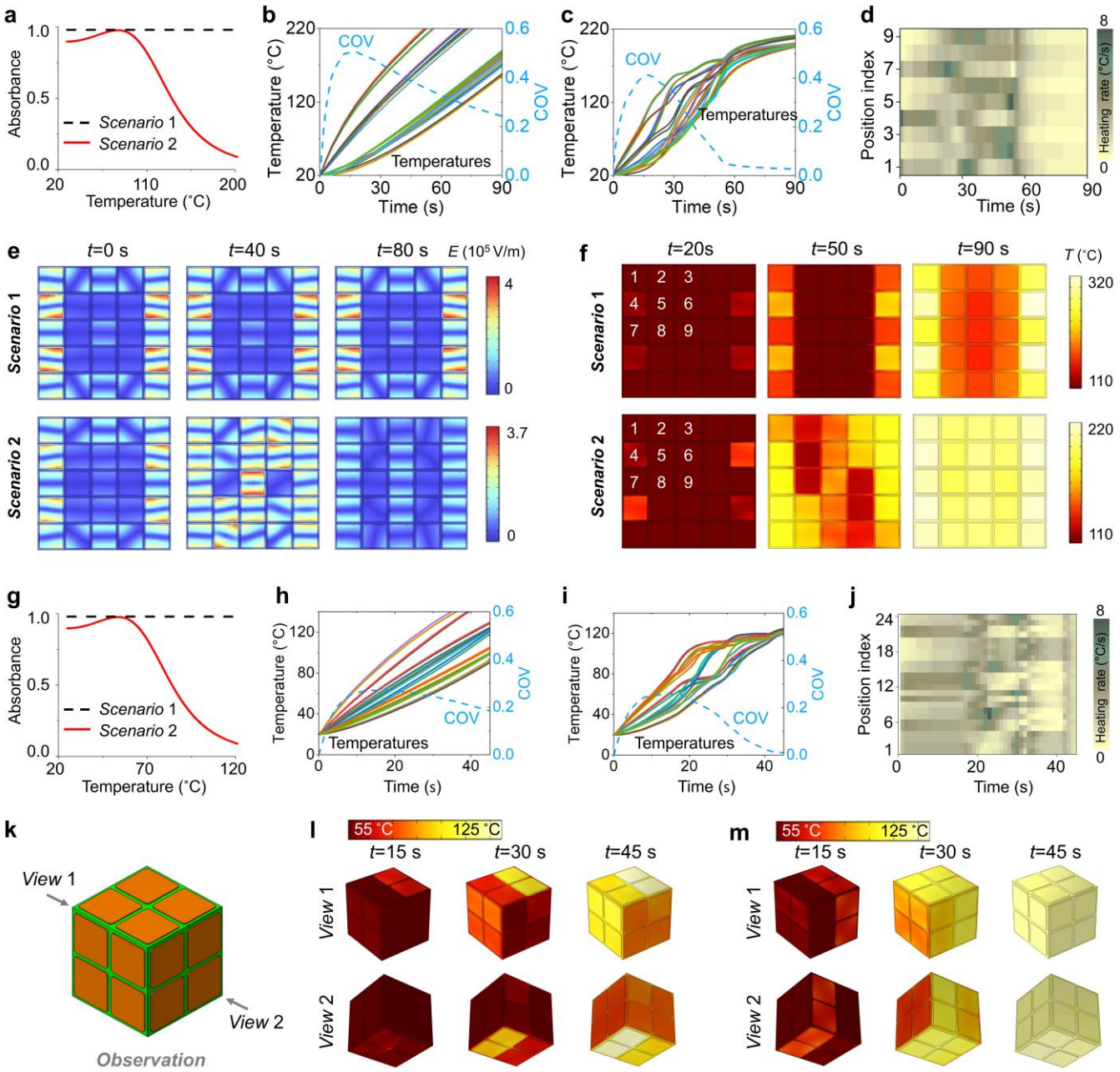

Figure 4| Simulation validation of enhanced heating uniformity enabled by the NTC MA. a *A*–*T* curves adopted in simulations for *Scenario* 1 and *Scenario* 2 in the planar configuration. **b**,**c** Temperature profiles of all MA units under *Scenario* 1 (**b**) and *Scenario* 2 (**c**). **d** Heating rates of 9 representative units located in one quarter of the MA under *Scenario* 2. **e** Temporal evolution of the electric field distribution (magnitude) inside the MA's dielectric spacer under *Scenario* 1 and *Scenario* 2. **f** Temporal evolution of the MA's surface temperature under *Scenario* 1 and *Scenario* 2. **g** *A*–*T* curves adopted in simulations for

Scenario 1 and *Scenario* 2 in the cubic configuration. **h**,**i** Temperature profiles of all units on the cubic MA under *Scenario* 1 (**h**) and *Scenario* 2 (**i**). **j** Heating rates of all units on the cubic MA under *Scenario* 2. **k** Geometry and spatial orientation of the cubic MA. **l**,**m** Temperature distributions on different cube faces under *Scenario* 1 (**l**) and *Scenario* 2 (**m**).

Figure 4g-m present the simulation results for the MA with a cubic configuration. As shown in **Figure 4g**, the *A*–*T* profile employed here resembles that in **Figure 4a**, but with a different target temperature, highlighting the design flexibility of the proposed approach. **Figure 4h** and **4i** provide a comparative analysis of the simulated temperature profiles for all units distributed across the six faces under *Scenario* 1 and *Scenario* 2, revealing trends consistent with those observed for the planar MA. Quantitatively, a 94% reduction in COV is achieved at $t = 47$ s, confirming the effectiveness of the adaptive heating pattern (**Figure 4j**). To visualize the thermal evolution on all six faces, simulated temperature distributions are shown from two distinct viewing perspectives (**Figure 4k**). As illustrated in **Figure 4l**, *Scenario* 1 yields time-invariant and highly non-uniform thermal patterns, with certain faces—particularly those oriented away from the microwave port (i.e., *View* 2)—remain substantially cooler throughout the process. In sharply contrast, *Scenario* 2 exhibits dynamic thermal evolution, resulting in significantly improved temperature uniformity, as depicted in **Figure 4m** and **Supplementary Movie 2**. Furthermore, **Supplementary Note 6** demonstrates similar findings for MAs with a dodecahedral configuration, where a two-stage NTC strategy (*Scenario* 2 *Plus*) is also validated via microwave-frequency tuning. In addition, demonstrations on MAs with a dielectric target object and in cavities with different sizes and geometries have been conducted. Collectively, these results substantiate the capability of the proposed method to effectively handle complex situations and accommodate multi-stage heating requirements encountered in practical applications.

Figure 5a presents a photograph of the fabricated NTC MA, in which a key advancement was the thermo-responsive permittivity engineering of the dielectric spacer. The dielectric spacer consists of two materials: polyimide films (thickness $N_1 d_1$), whose relative permittivity ε_1 remains stable from room

temperature to 120 °C, and organosilicon polymer films (thickness $N_2 d_2$), whose relative permittivity $\varepsilon_2(T)$ decreases monotonically with temperature over the same range (**Figure 5b**). According to effective medium theory, several NTC MAs with different thickness ratios (α) of organosilicon polymer films were fabricated, and their temperature-dependent absorption properties were measured. Further details regarding the design of the thermosensitive dielectric spacer and the microwave-absorption measurement setup are provided in **Supplementary Note 7**. As shown in **Figure 5c**, temperature-dependent absorption peaks with varying resonant frequency shift ranges were realized by tailoring the value of α. A constant MA with stable microwave absorption was fabricated when $\alpha = 0\%$, while two NTC MAs with resonant frequency shift ranges of 0.09 GHz and 0.30 GHz were obtained at $\alpha = 17\%$ and $\alpha = 50\%$, respectively. **Figure 5d** displays the measured *A*–*T* curves of the constant MA at 2.45 GHz (*Scenario* 1, $\alpha = 0\%$) and the NTC MA at 2.43 GHz (*Scenario* 2, $\alpha = 17\%$), which align closely with the results observed in the simulation (**Figure 4a**). Additionally, **Figure 5e** shows the *A*–*T* curve of the NTC MA with $\alpha = 50\%$, where two stages of NTC absorption are demonstrated by adjusting the microwave frequency from 2.40 GHz to 2.50 GHz at the beginning of the second stage (*Scenario* 2 *Plus*).

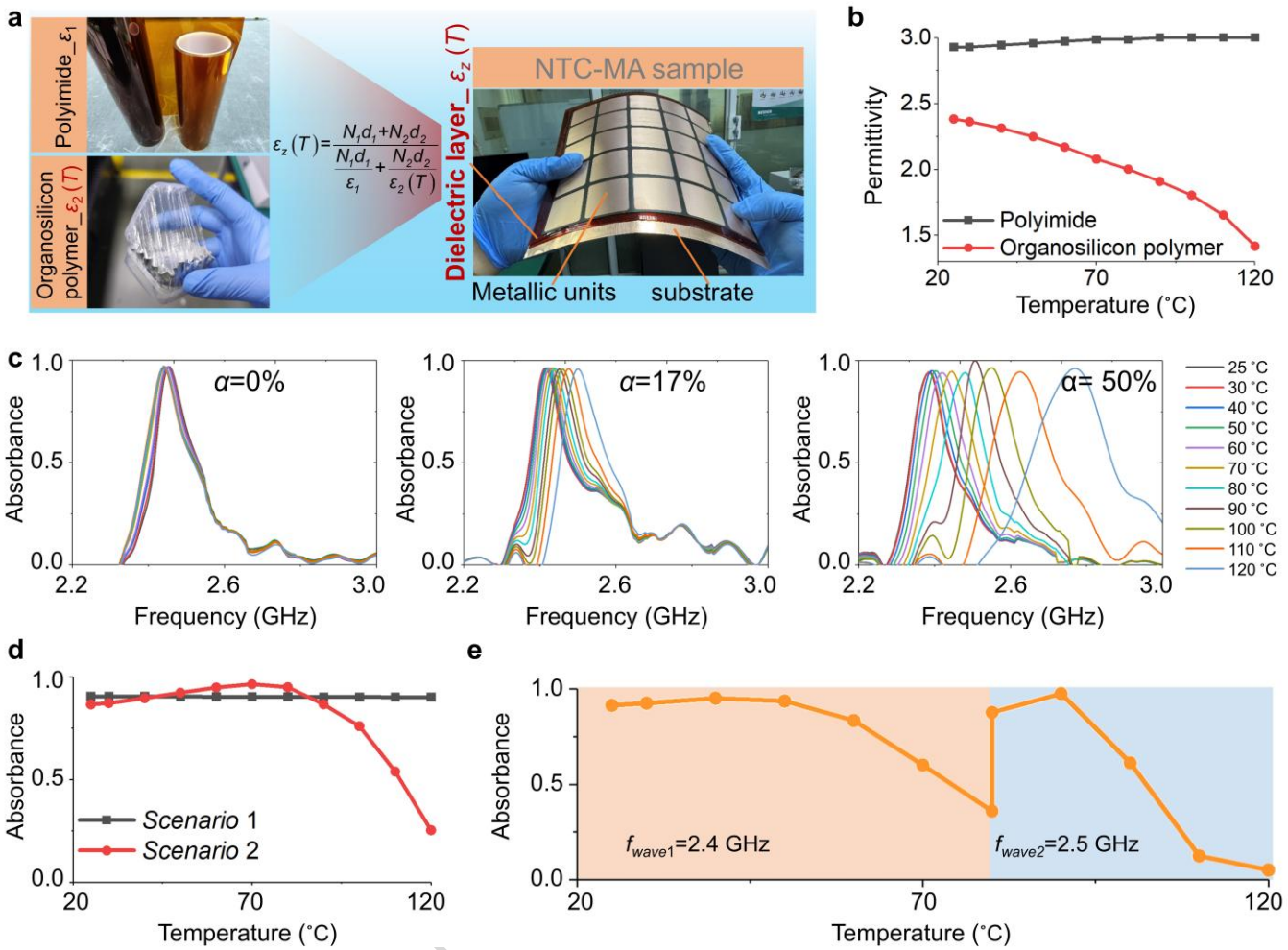

Figure 5| Sample fabrication and measurement. a Photograph of a fabricated NTC MA composed of thermostable (polyimide) and thermosensitive (organosilicon polymer) dielectric layers. **b** Temperature-dependent permittivity of the polyimide and organosilicon polymer films. **c** Temperature-dependent absorbance-frequency spectra of fabricated MAs with different α values. **d** Measured *A*–*T* curves for *Scenario* 1 and *Scenario* 2. **e** Measured *A*–*T* curves for *Scenario* 2 *Plus* showing two-stage NTC absorption at different frequencies.

Microwave heating experiments were conducted on the fabricated MAs in various configurations, with detailed experimental settings provided in **Supplementary Note 8**. The results for the planar MA are presented in **Figure 6a-e**. It can be observed that the experimental results exhibit excellent agreement with the simulations. Under *Scenario* 1, a distinctly non-uniform and fixed heating pattern is observed in both the infrared thermal images and the temporal temperature profiles, along with the corresponding heating rates derived from these profiles. In contrast, *Scenario* 2 demonstrates adaptive thermal regulation,

characterized by converging temperature trajectories, fluctuating heating rates, and dynamic temperature distributions. As a result, a 94% reduction in COV is achieved at $t = 6$ min compared to *Scenario* 1. A visual comparison of the complete thermal dynamics between these two scenarios is provided in **Supplementary Movie 3**. It should be noted, however, that the proposed strategy inevitably reduces heating efficiency compared with conventional microwave heating. To ensure a fair comparison, we define an energy-efficiency coefficient as the average temperature rise of the entire target per unit microwave power. At $t = 6$ min, the coefficient is 0.67 °C/W for *Scenario* 1 and 0.44 °C/W for *Scenario* 2, corresponding to a 34.3% decrease in energy efficiency for the NTC MA. This reduction stems intrinsically from the intentional suppression of microwave absorption at elevated temperatures. Nevertheless, such efficiency loss can be mitigated in practical implementations through complementary strategies, such as asymmetric waveguide configurations, as demonstrated in **Supplementary Note 5**.

The heating performance of the fabricated MAs in the cubic configuration is presented in **Figure 6f-l**. **Figure 6f** shows a photograph of the cubic MA and its arrangement within the microwave cavity, where dual infrared cameras simultaneously monitor the temperature distributions across all faces. Infrared thermal images depicting the evolution of the temperature field under *Scenario* 1 and *Scenario* 2 are presented in **Figure 6g** and **6h**, with the complete thermal dynamics documented in **Supplementary Movie 4.** As observed, *Scenario* 1 exhibits a stable and uneven temperature distribution, with some regions remaining nearly unheated. In contrast, *Scenario* 2 demonstrates an almost uniform temperature field. The lower-temperature regions circled in the images arise from heating dissipation through the microwave- reflective support base. The recorded temperature profiles and corresponding COV curves for both scenarios are presented in **Figure 6i** and **6j**. Compared to *Scenario* 1, *Scenario* 2 achieves a reduction of 93% in COV at $t = 10$ min. Moreover, we explored the influence of the arrangement of the NTC MA within the cavity. As shown in **Figure 6k** and **6l**, as well as in **Supplementary Movie 5**, *Scenario* 2 maintains consistent performance regardless of the position and orientation of the NTC MA,

confirming the robustness of our method. Note that the apparent hot spots around the cubic MA in **Supplementary Movies 4** and **5** are not actual temperature rises, but instead arise from infrared-signal reflections, as the metallic cavity walls behave as opposing mirrors that repeatedly reflect the emitted radiation.

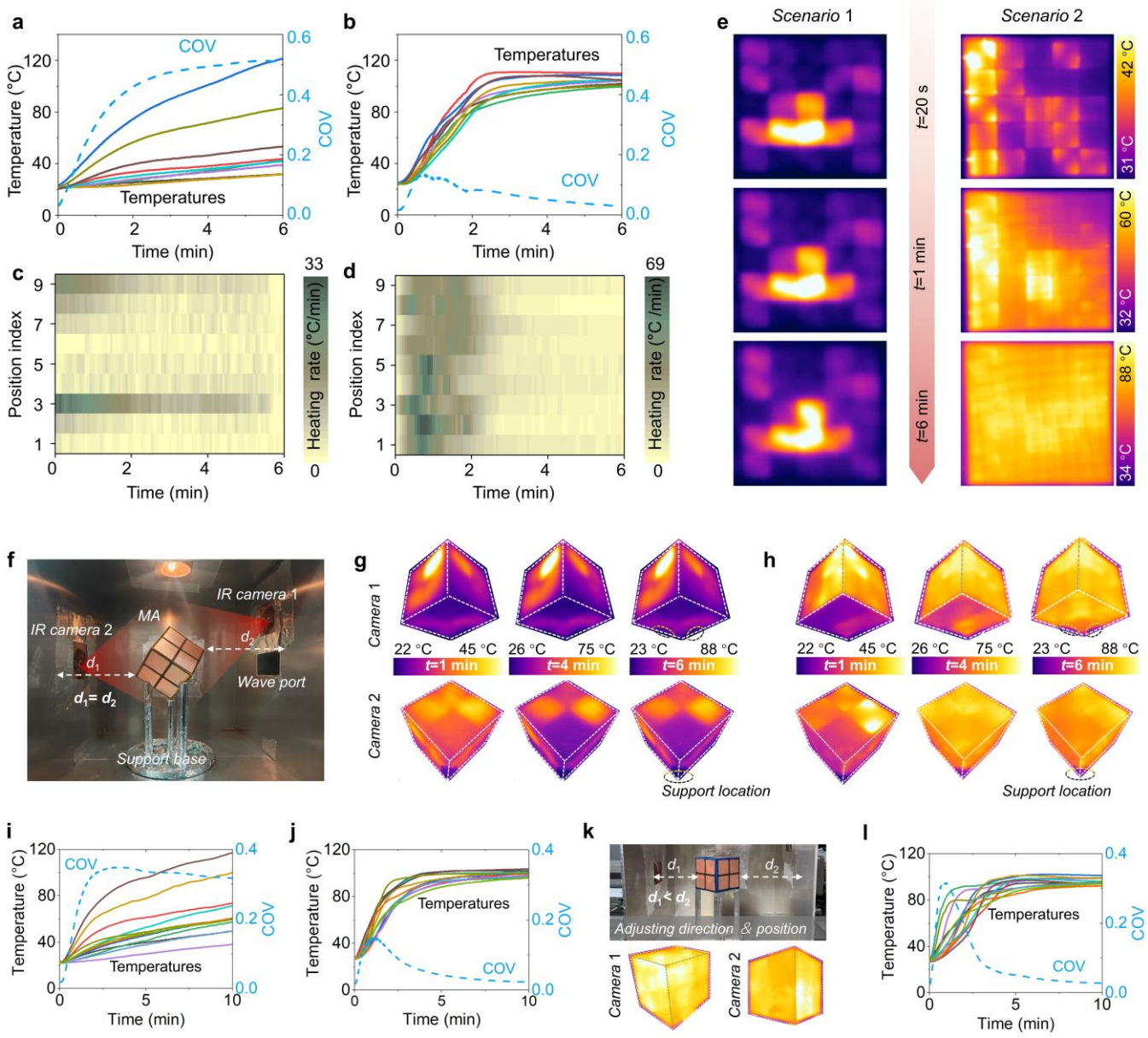

Figure 6| Experimental validation of enhanced heating uniformity enabled by the NTC MA. a,**b** Temperature profiles recorded at nine monitoring points, along with the associated COV curve, under *Scenario* 1 (**a**) and *Scenario* 2 (**b**) in the planar configuration. **c**,**d** Corresponding heating rates derived from the temperature profiles under *Scenario* 1 (**c**) and *Scenario* 2 (**d**). **e** Visual comparison of the thermal evolution between the two scenarios using infrared thermal imaging. **f** Photograph of the cubic MA and

its arrangement within the microwave cavity. **g**,**h** Infrared thermal images of the cubic MA under *Scenario* 1 (**g**) and *Scenario* 2 (**h**). **i**,**j** Recorded temperature profiles and the corresponding COV curve under *Scenario* 1 (**i**) and *Scenario* 2 (**j**) in the cubic configuration. **k** Photograph and infrared thermal images of the cubic NTC MA in another arrangement. **l** Recorded temperature profiles and the corresponding COV curve of the cubic NTC MA in another arrangement.

Beyond planar and polyhedral geometries, we further validated the effectiveness of the NTC MA on curved surfaces. As shown in **Figure 7a** and **7b**, the NTC MA is implemented on a cylindrical shell and a Möbius strip, representing directional and non-directional curvature, respectively. In both configurations, the NTC MA consistently achieves uniform microwave heating. The full thermal evolution is provided in **Supplementary Movie 6**, demonstrating the robustness of the approach against geometric deformation. It should be noted that apparent hot spots around the samples in the movie are artefacts caused by infrared reflections from the metallic cavity walls, as mentioned earlier. Furthermore, we validated the heating performance of the NTC MA after being cut into two smaller pieces (**Figure 7c**), which maintains uniform microwave heating and facilitates conformal integration with objects of more complex geometries.

Furthermore, simulations have been performed to investigate the potential of the NTC MA for programmable, pattern-selective uniform heating, which in this case requires dynamic tuning of the microwave frequency. As illustrated in **Figure 7d**, a planar NTC MA with a stacked-metasurface configuration is positioned at the center of a cubic microwave cavity with a side length of 300 mm. The MA consists of three types of units—MA_1, MA_2, and MA_3 (see **Figure 7e**)—containing three, two, and one metal–dielectric–metal layers along the normal direction, respectively, and therefore exhibiting three, two, and one resonant peaks in the absorbance–frequency spectra. Additional details regarding the MA configuration are provided in **Supplementary Note 4**. As shown in **Figure 7f** and **Supplementary Movie 7**, by tuning the microwave frequency to 2.04 GHz, 2.42 GHz, and 2.97 GHz, programmable pattern-selective heating is achieved, where the temperature distribution sequentially forms the Chinese characters "一", "十", and "田" (meaning "one," "ten," and "field," respectively). At each stage, uniform

temperature distribution within the target pattern is maintained, owing to the NTC absorption effect. This clearly demonstrates the strong programmability and versatility of the proposed approach.

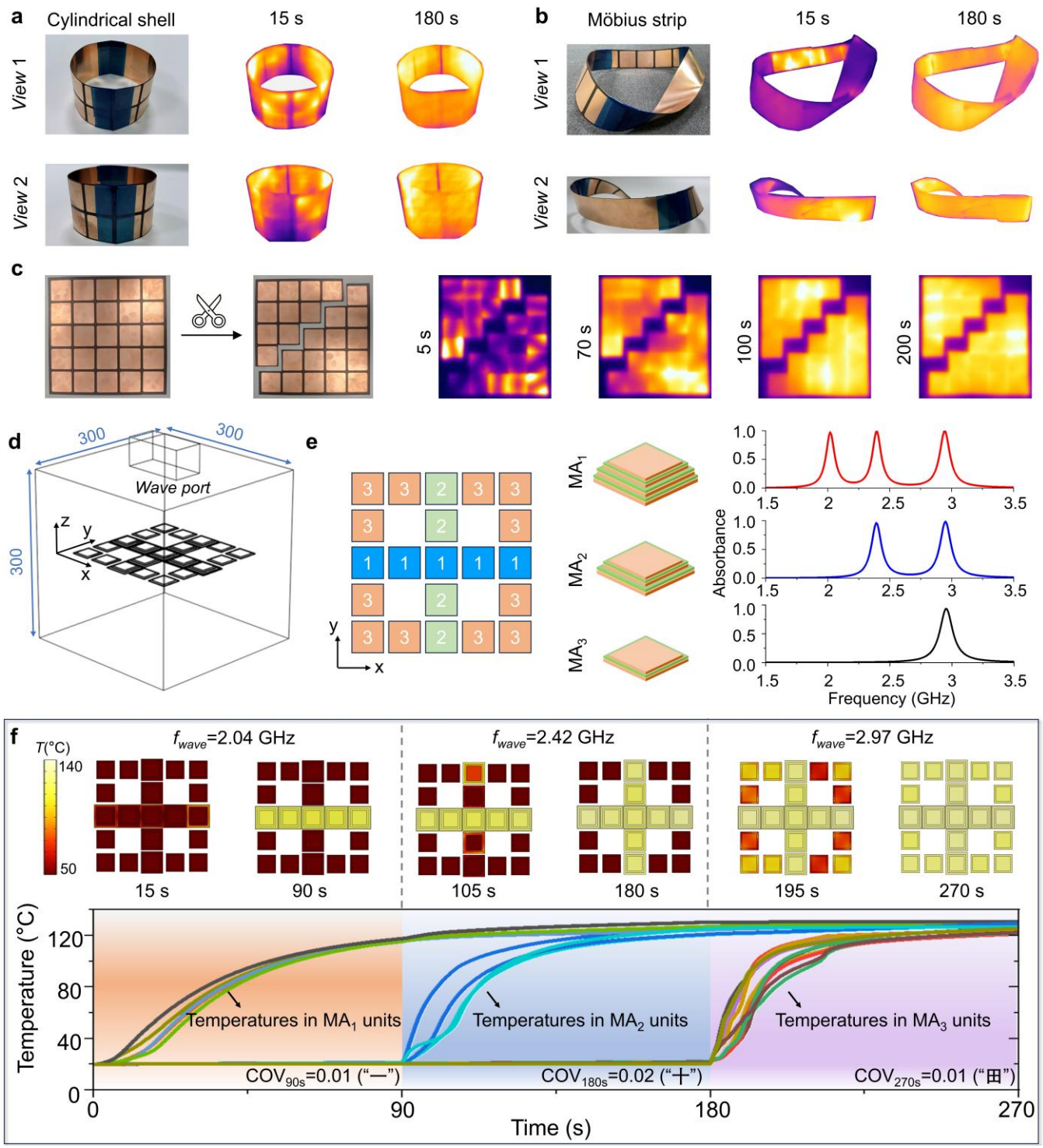

Figure 7| Uniform heating under geometric deformation, mechanical reconfiguration, and programmable pattern-selective heating enabled by NTC MAs. a Photographs and infrared images of a cylindrical shell. **b** Photographs and infrared images of a Möbius strip. **c** Photographs and infrared

images of an MA film after mechanical cutting into two pieces. **d** Simulation configuration for the programmable pattern-selective heating demonstration. **e** Schematic and absorbance spectra of the stacked NTC MA comprising MA_1, MA_2, and MA_3 units. **f** Sequential evolution of the dynamic heating patterns and the corresponding temperature profiles of each MA unit under frequency-selective excitation.

Finally, a representative application is showcased in **Supplementary Note 9**, where the developed NTC MA is applied to curing polymer composite structures. As expected, the enhanced temperature uniformity ensures uniform curing in all tested structures, including a planar laminate, a wing leading-edge panel, and a cylindrical shell.

Limit analysis of NTC MAs in enhancing microwave heating uniformity

To verify the effectiveness of the method under extreme conditions, simulation studies were carried out within a single-mode cavity (**Figure 8a**). As is well known, single-mode cavities not only exhibit the most uneven electromagnetic field (with the strongest intensity at the center and zero at the edges) but also maintain a fixed field pattern, thereby eliminating contributions from field redistribution effects. Thus, they represent the extreme case in this study. As shown in **Figure 8b**, the step-like *A*–*T* curve was adopted in *Scenario* 2 to ensure the optimal performance of the proposed method. However, a residual absorbance of approximately 4.8% beyond the target temperature of 120 °C is unavoidable due to the intrinsic absorption of the dielectric spacer. Detailed simulation settings are provided in **Supplementary Note 4**.

As depicted in **Figure 8c**, under *Scenario* 1, the temperature curves on each MA unit initially diverge and then become parallel under the influence of thermal conduction. In contrast, *Scenario* 2 displays temperature profiles that diverge initially but tend to converge toward the target temperature (**Figure 8d**). Nevertheless, the COV does not ultimately reach zero, owing to the aforementioned residual absorbance. Even so, a 90% reduction in COV is achieved at $t = 52$ s under this extreme condition. As illustrated in **Figure 8e** and **8f**, the electric field distribution within the dielectric spacer of the constant MA is consistently maintained in the form of a typical single-mode pattern, resulting in a highly non-uniform, sinusoidal temperature distribution. By comparison, the initially non-uniform electric field distribution

within the NTC MA becomes progressively more uniform, accompanied by a gradual decline in overall field intensity. Correspondingly, the temperature field evolves from an initially uniform state (room temperature) to a non-uniform state during the heating process, and ultimately returns to uniformity at the target temperature.

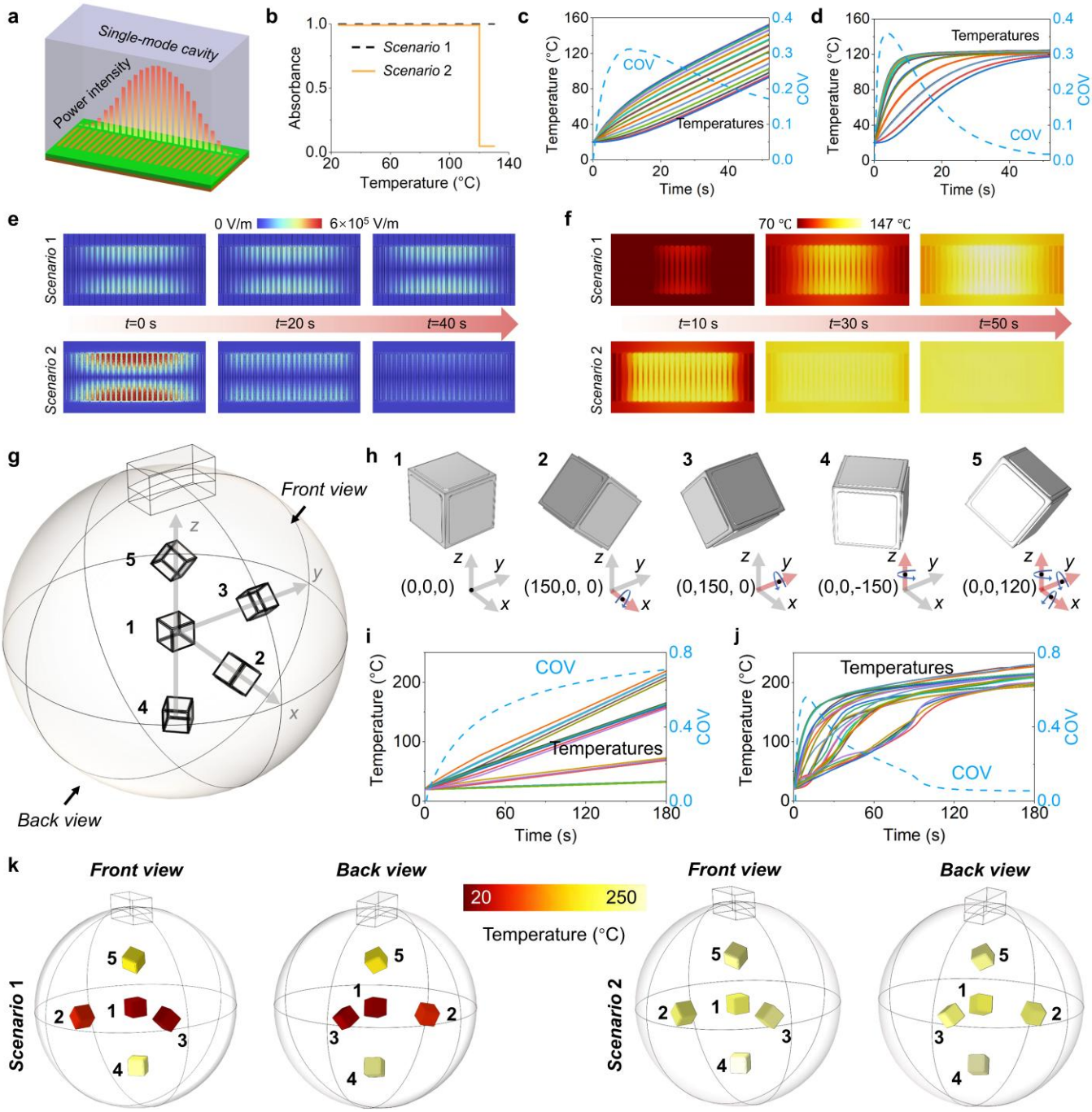

Figure 8| Limit analysis of NTC MAs in enhancing microwave heating uniformity. a-f Simulation results within a single-mode cavity. **a** Illustration of the simulation configuration. **b** Adopted *A*–*T* curves

for *Scenario* 1 and *Scenario* 2. **c**,**d** Temperature profiles on all MA units and the corresponding COV curve under *Scenario* 1 (**c**) and *Scenario* 2 (**d**). **e** Temporal evolution of the electric field distribution (magnitude) within the dielectric spacer under both scenarios. **f** Temporal evolution of the surface temperature field under both scenarios. **g-k** Simulation results within the spherical multimode cavity. **g** Spatial arrangement of five cubic MAs inside the cavity. **h** Spatial orientation of each MA. **i**,**j** Temperature profiles across six faces of the five cubic MAs under *Scenario* 1 (**i**) and *Scenario* 2 (**j**). **k** Final temperature distributions on the five MAs under both scenarios.

Moreover, microwave heating simulations involving multiple objects were also conducted within a spherical multimode cavity characterized by highly uneven electromagnetic field distributions. **Figure 8g** and **8h** illustrate the spatial arrangement and orientation of five cubic MAs inside the cavity. Specifically, MA-1, MA-4, MA-5, and the wave port were deliberately aligned along a diameter of the spherical cavity, resulting in pronounced mutual occlusion. MA-2, and MA-3 were placed on the equatorial plane to represent two distinct spatial offset configurations relative to the wave port. In addition, each MA was subjected to a controlled 45° rotation about different axes to thoroughly assess the robustness of our method. More simulation details can be found in **Supplementary Note 4**.

For comprehensive thermal analysis, temperature distributions were examined from both front and back perspectives. **Figure 8i** and **8j** present the temperature profiles across all six faces of the five cubic MAs under *Scenario* 1 and *Scenario* 2, respectively. Under *Scenario* 1, the temperature profiles still exhibit continuous divergence over time, while under *Scenario* 2, the initially diverging profiles progressively converge toward the target temperature, resulting in a 92% reduction in COV at $t = 180$ s. A visual comparison of the thermal evolution in both scenarios is available in **Supplementary Movie 8**, with the final temperature distribution shown in **Figure 8k**. These results clearly demonstrate the robustness and generalizability of our method. In the future, the proposed method could be further integrated with existing techniques—for example, electromagnetic field control and heat transfer optimization—to enable fully uniform heating across diverse application scenarios. Furthermore, the

developed NTC MA concept may be extended to other electromagnetic frequency bands for adaptive wave absorption.

Methods

Simulation settings

Electromagnetic–thermal coupling simulations were performed using COMSOL Multiphysics. Detailed configurations for the field-redistribution analysis, the heating of planar and polyhedral structures, the programmable pattern-selective heating in multimode cavities, and the limit-analysis simulations are provided in **Supplementary Note 4**.

Experiment settings

Details of the microwave-absorption measurements are given in **Supplementary Note 7**. The experimental setups for microwave heating of planar and cubic objects, as well as for the cylindrical shell and Möbius strip, are described in **Supplementary Note 8.**

Data availability

Data supporting the findings of this study are provided in the Source Data file.

References

1. Huang, M. et al. Fast microwave heating-based one-step synthesis of DNA and RNA modified gold nanoparticles. Nat. Commun. 13, 968 (2022).
2. Jie, X. et al. Microwave-initiated catalytic deconstruction of plastic waste into hydrogen and high-value carbons. Nat. Catal. 3, 902-912 (2020).
3. Sweeney, C. B. et al. Welding of 3D-printed carbon nanotube–polymer composites by locally induced

microwave heating. Sci. Adv. 3, e1700262 (2017).

4. Zhong, G. et al. Synthesis of metal oxide nanoparticles by rapid, high-temperature 3D microwave heating. Adv. Funct. Mater. 29, 1904282 (2019).
5. Wu, Y., Mu, R., Li, G., Li, M. & Lv, W. Research progress in fluid and semifluid microwave heating technology in food processing. Compr. Rev. Food. Sci. Food Saf. 21, 3436-3454 (2022).
6. An, N., Li, D., Wang, L. & Wang, Y. Factors affecting energy efficiency of microwave drying of foods: an updated understanding. Crit. Rev. Food Sci. Nutr. 64, 2618-2633 (2024).
7. Kishimoto, F. et al. Direct microwave energy input on a single cation for outstanding selective catalysis. Sci. Adv. 9, eadi1744 (2023).
8. Borkar, S. S., Vito, J. & Shetty, M. Microwave-heated solvent extraction and catalysis for end-of-life tire decontamination. Nat. Chem. Eng. 1, 561-562 (2024).
9. Kwak, Y. et al. Microwave-assisted, performance-advantaged electrification of propane dehydrogenation. Sci. Adv. 9, eadi8219 (2023).
10. Xiao, S. et al. A chloroplast structured photocatalyst enabled by microwave synthesis. Nat. Commun. 10, 1570 (2019).
11. Zhou, J. et al. Microwave heating and curing of metal-like CFRP laminates through ultrathin and flexible resonance structures. Compos. Sci. Technol. 218, 109200 (2022).
12. Zhao, J. et al. Highly selective upcycling of plastic mixture waste by microwave-assisted catalysis over Zn/b-ZnO. Nat. Commun. 16, 1726 (2025).
13. Alhashim, S. H., Bhattacharyya, S. & Ajayan, P. M. Microwave assisted ultrafast, selective lithium extraction in deep eutectic solvent for LIB cathode recycling. Adv. Funct. Mater. 34, 2404570 (2024).
14. Gao, Y., Liu, Y. & Zou, D. Microwave-assisted synthesis and environmental remediation: a review. Environ. Chem. Lett. 21, 2399-2416 (2023).
15. Soldatov, S. et al. Time-resolved optical emission spectroscopy reveals nonequilibrium conditions for CO_2 splitting in atmospheric plasma sustained with ultrafast microwave pulsation. ACS Energy

Lett. 6, 124-130 (2021).

16. Serra, J. M. et al. Hydrogen production via microwave-induced water splitting at low temperature. Nat. Energy 5, 910-919 (2020).
17. Ren, X. et al. Challenges and opportunities in microwave-assisted catalytic pyrolysis of biomass: A review. Appl. Energy 315, 118970 (2022).
18. Wu, Y. et al. Thermal-responsive activation of engineered bacteria to trigger antitumor immunity post microwave ablation therapy. Nat. Commun. 15, 1-19 (2024).
19. Zhu, Y. et al. Metallo-alginate hydrogel can potentiate microwave tumor ablation for synergistic cancer treatment. Sci. Adv. 8, eabo5285 (2022).
20. Valverde, C., Rodríguez-García, M. M., Rojas, E., & Bayón, R. State of the art of the fundamental aspects in the concept of microwave-assisted heating systems. Int. Commun. Heat Mass 156, 107594 (2024).
21. Mgbemena, C. O. et al. Accelerated microwave curing of fibre-reinforced thermoset polymer composites for structural applications: A review of scientific challenges. Compos. Pt. A-Appl. Sci. Manuf. 115, 88-103 (2018).
22. Goyal, H., Chen, T. Y., Chen, W. & Vlachos, D. G. A review of microwave-assisted process intensified multiphase reactors. Chem. Eng. J. 430, 133183 (2022).
23. Yang, R., Fathy, A. E., Morgan, M. T. & Chen, J. Development of online closed-loop frequency shifting strategies to improve heating performance of foods in a solid-state microwave system. Food Res. Int. 154, 110985 (2022).
24. Ahn, S. H., Jeong, C. H., Lim, D. M. & Lee, W. S. Kilowatt-level power-controlled microwave applicator with multiple slotted waveguides for improving heating uniformity. IEEE Trans. Microw. Theory Tech. 68, 2867-2875 (2020).
25. Wang, L. et al. Modeling the RF heating uniformity contributed by a rotating turntable. J. Food Eng. 339, 111289 (2023).

26. Wang, Y., Yang, X. & Qiu, Y. Double pendulum mode stirrer for improved multimode microwave heating performance. Int. J. RF Microw. C. E. 31, e22866 (2021).
27. Zhou, J. et al. A multi-pattern compensation method to ensure even temperature in composite materials during microwave curing process. Compos. Part A-Appl. S. 107, 10-20 (2018).
28. Zhou, J., Li, Y., Li, D. & Wen, Y. Online learning based intelligent temperature control during polymer composites microwave curing process. Chem. Eng. J. 370, 455-465 (2019).
29. Wang, J. et al. Improvement of microwave heating efficiency and uniformity by controllable rotary columns array. IEEE Trans. Microw. Theory Tech. 71, 3517-3529 (2023).
30. Kim, D. et al. Enhancing microwave heating uniformity using reconfigurable diffractive beamforming surface. Microw. Opt. Techn. Let. 64, 47-53 (2022).
31. Landy, N. I., Sajuyigbe, S., Mock, J. J., Smith, D. R. & Padilla, W. J. Perfect Metamaterial Absorber. Phys. Rev. Lett. 100, 207402 (2008).
32. Shrekenhamer, D., Chen, W. C. & Padilla, W. J. Liquid crystal tunable metamaterial absorber. Phys. Rev. Lett. 110, 177403 (2013).
33. Qu, S., Hou, Y. & Sheng, P. Conceptual-based design of an ultrabroadband microwave metamaterial absorber. P. Natl. Acad. Sci. USA 118, e2110490118 (2021).
34. Zhang, C. et al. Hybrid metamaterial absorber for ultra-low and dual-broadband absorption. Opt. Express 29, 14078-14086 (2021).
35. Zhou, J. et al. Zone-regulated microwave heating of CFRP laminates via ultrathin and flexible resonance structures with different working frequencies. Compos. Commun. 29, 101016 (2022).
36. Wang, B. X., Xu, C., Duan, G., Xu, W. & Pi, F. Review of broadband metamaterial absorbers: from principles, design strategies, and tunable properties to functional applications. Adv. Funct. Mater. 33, 2213818 (2023).
37. Li, D. et al. Microwave heating of carbon materials for on-demand thermal patterning via tunable electromagnetic resonators. Carbon 203, 865-875 (2023).

38. Yu, N. & Capasso, F. Flat optics with designer metasurfaces. Nat. Mater. 13, 139-150 (2014).
39. Cui, T. J. et al. Roadmap on electromagnetic metamaterials and metasurfaces. J. Phys.-Photonics 6, 032502 (2024).
40. Davies, B. et al. Roadmap on metamaterial theory, modelling and design. J. Phys. D Appl. Phys. 58, 203002 (2025).
41. Kuznetsov, A. I. et al. Roadmap for optical metasurfaces. ACS photonics 11, 816-865 (2024).
42. Zaidi, A. et al. Metasurface-enabled single-shot and complete Mueller matrix imaging. Nat. Photonics 18, 704-712 (2024).
43. Oudich, M., Kong, X., Zhang, T., Qiu, C. & Jing, Y. Engineered moiré photonic and phononic superlattices. Nat. Mater. 23, 1169-1178 (2024).
44. Jiang, G. et al. Abnormal beam steering with kirigami reconfigurable metasurfaces. Nat. Commun. 16, 1660 (2025).
45. Wu, H. et al. A programmable metasurface antenna that approaches the wireless information mapping limit. Nat. Electron. 8, 179-191 (2025).
46. Yang, J. et al. Transmission-reflection-integrated programmable metasurface for simultaneous and independent control of bidirectional incident waves. Adv. Funct. Mater., 2419681 (2025).
47. Dorrah, A. H., Park, J. S., Palmieri, A. & Capasso, F. Free-standing bilayer metasurfaces in the visible. Nat. Commun. 16, 3126 (2025).
48. Li, D. et al. A generalized equivalent circuit model for composite metamaterial absorbers: From isotropic to anisotropic substrate. Compos. Sci. Technol. 257, 110832 (2024).
49. Li, Z., Haigh, A., Soutis, C. & Gibson, A. X-band microwave characterisation and analysis of carbon fibre-reinforced polymer composites. Compos. Struct. 208, 224-232 (2019).
50. Link, G. & Ramopoulos, V. Simple analytical approach for industrial microwave applicator design. Chem. Eng. Process. 125, 334-342 (2018).
51. Xu, Y. et al. Broadband asymmetric waveguiding of light without polarization limitations. Nat.

Commun. 4(1):2561 (2013).

52. Yang, F., Zhu, H., Yang, Y. & Huang, K. High-efficiency continuous-flow microwave heating system based on asymmetric propagation waveguide. IEEE Trans. Microw. Theory Tech. 70(3): 1920-1931 (2021).

Acknowledgements

We thank Prof. Ke XU (NUAA), Prof. Huachen CUI (HKUST), and Prof. Huacheng ZHU (SCU) for their valuable discussions.

Funding Statement

This project was funded by the Major Program of the National Natural Science Foundation of China (Grant no. 52090052), the Jiangsu Provincial Key Basic Research Program (Grant No. BK20253022), the National Science Fund for Distinguished Young Scholars (Grant no. 51925505), the Fundamental and Interdisciplinary Disciplines Breakthrough Plan of the Ministry of Education of China (Grant no. JYB2025XDXM205), the National Natural Science Foundation of China (Grant no. U2570244, 52405377 and 52105364), and the New Cornerstone Science Foundation through the XPLORER PRIZE.

Author contributions

J.Z. and D.L. contributed equally to this work. J.Z., D.L., and Y.L. conceived the concept; J.Z., D.L., L.Z., and G.L. conducted the theoretical analysis; J.Z. and D.L. designed the prototype setup; J.Z., D.L. and S.L. conceived the simulation and experiment; D.L. and L.X. conducted the simulation; D.L., L.X. and X.C.H. conducted the experiment; J.Z., D.L., L.X., X.C.H., S.L., and X.Z.H. analyzed data; D.L. and J.Z. wrote the manuscript; J.G., G.L., L.Z., and Y.L. revised the manuscript; Y.L., L.Z., X.Z.H. supervised the project; Y.L., X.Z.H, J.Z. and S.L. acquired the funding. All authors discussed the results and commented on the manuscript.

Competing interests

The authors declare no competing interests.